

The protoMIRAX hard X-ray imaging balloon experiment

João Braga, Flavio D'Amico, Manuel A. C. Avila, Ana V. Penacchioni, J. Rodrigo Sacahui, Valdivino A. de Santiago Jr., Fátima Mattiello-Francisco, Cesar Strauss, and Márcio A. A. Fialho

National Institute of Space Research – INPE, Av. dos Astronautas 1758, 12227–010 São José dos Campos, SP, Brazil
e-mail: joao.braga@inpe.br

Received 17 April 2015 / Accepted 22 May 2015

ABSTRACT

Context. The protoMIRAX hard X-ray imaging telescope is a balloon-borne experiment developed as a pathfinder for the MIRAX satellite mission. The experiment consists essentially in a coded-aperture hard X-ray (30–200 keV) imager with a square array (13×13) of 2 mm-thick planar CZT detectors with a total area of 169 cm^2 . The total, fully-coded field-of-view is $21^\circ \times 21^\circ$ and the angular resolution is $1^{\circ}43'$.

Aims. The main objective of protoMIRAX is to carry out imaging spectroscopy of selected bright sources to demonstrate the performance of a prototype of the MIRAX hard X-ray imager. In this paper we describe the protoMIRAX instrument and all the subsystems of its balloon gondola, and we show simulated results of the instrument performance.

Methods. Detailed background and imaging simulations were performed for protoMIRAX balloon flights. The 3σ sensitivity for the 30–200 keV range is $\sim 1.9 \times 10^{-5} \text{ photons cm}^{-2} \text{ s}^{-1}$ for an integration time of 8 h at an atmospheric depth of 2.7 g cm^{-2} and an average zenith angle of 30° . We developed an attitude-control system for the balloon gondola and new data handling and ground systems that also include prototypes for the MIRAX satellite.

Results. We present the results of Monte Carlo simulations of the camera response at balloon altitudes, showing the expected background level and the detailed sensitivity of protoMIRAX. We also present the results of imaging simulations of the Crab region.

Conclusions. The results show that protoMIRAX is capable of making spectral and imaging observations of bright hard X-ray source fields. Furthermore, the balloon observations will carry out very important tests and demonstrations of MIRAX hardware and software in a near space environment.

Key words. stars: black holes – balloons – instrumentation: detectors – methods: laboratory: solid state – telescopes – space vehicles: instruments

1. Introduction

Coded mask experiments have been widely used in astronomical hard X-ray ($E \gtrsim 10 \text{ keV}$) observations of the sky due to several factors. First, the technology for developing focusing telescopes above these energies has only recently been mastered and implemented, especially in the NuSTAR observatory (Harrison et al. 2013). The ASTRO-H mission, expected to be launched in the near future, will also make use of focusing optics in the hard X-ray range through its Hard X-ray Telescope (HXT; Takahashi et al. 2014). While providing much higher sensitivities and better angular resolution in general, these instruments require very long focal lengths and sophisticated control and alignment systems. In addition, the highest energy achievable is still significantly below 100 keV, even though there are promising higher energy ($\lesssim 600 \text{ keV}$) focusing techniques such as the Laue lenses being developed (Virgilli et al. 2013). Coded mask instruments, on the other hand, allow imaging over very wide fields of view (which can be a significant portion of the sky) and up to energies of several hundred keV. Another factor is that coded mask instruments can be compact and easy to implement, making them good options for wide-field hard X-ray and low-energy γ -ray monitors of the highly variable and transient source populations in this energy range. Important examples of coded mask satellite instruments that have made significant contributions to astronomy are the SIGMA (Paul et al. 1991) and ART-P (Sunyaev et al. 1990) instruments onboard GRANAT, the ASM on RXTE

(Levine et al. 1996), the WFCs on *BeppoSAX* (Jager et al. 1997), the WFM on HETE-2 (Ricker et al. 2003), instruments on the INTEGRAL satellite (Winkler 1995), and *Swift*/BAT (Gehrels & Swift Team 2004).

In this paper we describe the protoMIRAX balloon experiment, a wide-field hard X-ray coded mask imager under development at the National Institute for Space Research (INPE) as a pathfinder for the MIRAX (Monitor e Imageador de Raios X) satellite mission (Braga et al. 2004). The main instrument of the balloon payload is a hard X-ray camera that employs an array of 13×13 CdZnTe (CZT) detectors as the position-sensitive detector plane. The experiment will be launched on a stratospheric balloon over Brazil at a latitude of $\sim 23^\circ \text{ S}$ to carry out imaging spectroscopy of selected bright sources. In addition to testing the camera performance in a near-space environment, the experiment is a testbed for new space technologies being developed at INPE. A new attitude control and pointing system for scientific balloon gondolas, including two new star trackers, will be tested, as well as novel data handling and ground support systems.

In Sect. 2 we present the scientific objectives of the experiment. In Sect. 3 we describe the X-ray camera and the other subsystems that protoMIRAX comprises. In Sect. 4 we present the results of Monte Carlo simulations of the camera response at balloon altitudes, showing the expected background level and the detailed sensitivity of protoMIRAX. A simulated image of the Crab region is shown in Sect. 5. We present our conclusions in Sect. 6.

2. Scientific objectives

The protoMIRAX experiment will perform imaging spectroscopy with good energy resolution of bright Galactic hard X-ray sources such as the Crab nebula (and its pulsar) and the Galactic center complex.

In X-ray astronomy, the Crab has been considered as a standard candle owing to its large and nearly constant flux at Earth (see Bühler & Blandford 2014; and Madsen et al. 2015, for recent reviews). At X-ray energies above ~ 30 keV, the Crab is generally the strongest persistent source in the sky, and it has a diameter of ~ 1 arcmin. The Crab has experienced some recent flares in the GeV range (Tavani et al. 2011) that were simultaneous or just previous to a particularly active period in hard X-rays (Wilson-Hodge et al. 2011). Those surprising variations represent a few percent of the persistent flux on the 50–100 keV energy range. ProtoMIRAX will be able to measure the Crab spectrum from 30 to 200 keV. These observations will also be used for flux calibrations and imaging demonstrations.

The Galactic center (GC) region is very favorable for protoMIRAX observations thanks to its declination of $\delta \sim -29^\circ$, since the balloon will fly over a region at latitudes of $\sim -23^\circ$. One of the most interesting sources is 1E 1740.7–2942, the brightest and hardest persistent X-ray source within a few degrees of the GC. Because of a similar hard X-ray spectrum and comparable luminosity to Cygnus X-1 (Liang & Nolan 1984), 1E 1740.7–2942 is classified as a black hole candidate. Because of the two-sided radio jets associated to the source, the object was dubbed the first “microquasar” (Mirabel et al. 1992), an X-ray binary whose behavior mimics quasars on a much smaller scale. Since the GC direction has extremely high extinction, a counterpart has not yet been identified despite deep searches in both the optical and IR bands. The source was recently studied by our group from soft to hard X-rays up to 200 keV (Castro et al. 2014), showing spectra that can be modeled very well by thermal Comptonization of soft X-ray photons. We will image the Galactic center region with protoMIRAX with 1E 1740.7–2942 in the center of the field of view (FOV). Our observations in the hard X-ray band could be useful for measuring flux and spectral parameters, especially because the source is in the hard state most of the time.

Another interesting source that will be in the same FOV is GRS 1758–258, also a microquasar, and one of the brightest X-ray sources near the GC at energies greater than 50 keV (Sunyaev et al. 1991a). Like its sister source 1E 1740.7–2942, GRS 1758–258 spends most of the time in the hard state. Its hard X-ray spectra and variability are also similar to Cyg X-1 (Kuznetsov et al. 1996). GRS 1758–258 also does not have an identified counterpart yet, so its mass and orbital periods are still unknown. The protoMIRAX observations will in principle be capable of attaining spectral and flux information about GRS 1758–258.

The GC field to be observed by protoMIRAX will also include GX 1+4, the best studied accreting pulsar around the GC, with a pulse period on the order of two minutes. This object is the prototype of the small but growing subclass of slowly rotating accreting X-ray pulsars called symbiotic X-ray binaries (SyXB), in which a neutron star accretes from the wind of an M-type giant companion (Masetti et al. 2006). GX 1+4 is a persistent source, but with strong, irregular flux variations on various timescales and extended hard/low states. Its peculiar spin history has been the object of intensive study (Nagase 1989), and Makishima et al. (1988) have shown a clear transition from spin-up to spin-down behavior in the equilibrium period,

characterizing a torque-reversal episode. More recent studies (González-Galán et al. 2012) have used data from *BeppoSAX*, *INTEGRAL*, *Fermi* and *Swift*/BAT to show that the source continues its spin-down trend with a constant change in frequency, and the pulse period has increased by $\sim 50\%$ over the past three decades. Since the source is highly variable, our spectral and timing observations can possibly contribute to the flux and period histories for this peculiar object.

Besides providing new data on astrophysical sources, the experiment will be able to make precise measurements of the hard X-ray background at balloon altitudes for the Brazilian mid-latitudes, which is important for investigating the South Atlantic Anomaly (SAA) and Space Weather phenomena.

3. The protoMIRAX experiment

The protoMIRAX experiment consists basically in a hard X-ray imaging camera mounted in a stratospheric balloon gondola capable of carrying out pointing observations of selected target regions. Table 1 presents an overview of the experiment’s baseline parameters.

3.1. The X-ray camera

The X-ray camera (XRC) is a coded-aperture wide-field hard X-ray imager that consists in an aluminum tower-like structure that supports an array of X-ray detectors, a collimator, a coded mask, passive shields and other electrical shielding and supporting components. In this section we describe each component of the XRC in detail.

3.1.1. The X-ray detectors

The X-ray detectors we use in this experiment are band-gap, room-temperature semiconductors made of an alloy of 90% cadmium telluride (CdTe) and 10% zinc telluride (ZnTe), called CdZnTe or simply CZT. They have high photoelectric efficiency up to hundreds of keV, owing to the high atomic numbers of Cd ($Z = 48$) and Te ($Z = 52$) and a density of 6 g cm^{-3} . The probability of photoelectric absorption per unit pathlength is roughly a factor of 4 to 5 times higher than in Ge for typical gamma-ray energies. The relatively large band gap of 1.5 eV precludes significant thermal excitations at room temperature and provides good enough energy resolution ($\Delta E/E \lesssim 10\%$ at 60 keV).

CZT detectors have often been used in X-ray astronomy because of their high efficiency with small thickness (thus reducing background, which scales with volume) and relative ease of handling and mounting. This allows for tiling so that large nearly-contiguous detector planes can be built.

The experiment uses 169 CZT detectors with platinum planar contacts and dimensions of $10 \text{ mm} \times 10 \text{ mm}$, thickness of 2 mm each, out of 200 units acquired from eV Products, USA. They will be configured in a 13×13 array, so the total area of the detector plane is 169 cm^2 . Owing to physical mounting restrictions, the edges of adjacent detectors will be separated by 10 mm. The operational energy range will be from 30 to 200 keV. The lower limit is determined by absorption in the residual atmosphere above balloon altitudes ($\sim 42 \text{ km}$), whereas the higher limit is determined by detector photoelectric efficiency given its thickness.

Each detector is connected directly to a printed circuit board (PCB) that carries the front-end analog electronics with a preamp, a low-noise amplifier (LNA) and a shaper. The PCBs

Table 1. ProtoMIRAX baseline parameters.

Detector system	
Detector type: CdZnTe (CZT) with platinum planar contacts	Dimensions: 10 mm × 10 mm × 2 mm (thickness)
Number of detectors: 169 (13 × 13)	Gap between detectors: 10 mm
Energy range: 30–200 keV	Geometrical area: 169 cm ²
Effective area @ 80 keV: 52 cm ² (through mask, at 2.7 g cm ⁻²)	Time resolution: 5 μs
Collimator	
Blade material: Cu (0.5 mm), Pb (0.5 mm), Cu (0.5 mm)	Cell size: squares of 20-mm sides
Blade height: 81 mm	External envelope: 260 mm × 260 mm × 81 mm
Coded mask	
Material: 1 mm-thick lead	Open fraction: 0.497
Basic pattern: 13 × 13 MURA	Element size: 20 mm × 20 mm
Extended pattern: 2 × 2 basic (minus 1 line and 1 column)	Total mask dimensions: 500 mm × 500 mm × 3 mm (total thickness)
Position: 650 mm from detector plane	(includes 2mm-thick acrylic substrate)
Shielding	
Material: lead (external – 1.5 mm), copper (internal – 0.5 mm)	Position: around detectors and collimator (sides and bottom)
Imaging parameters	
Angular resolution: 1°43'	Total (fully-coded) FOV: 21° × 21°
Source location accuracy: 10' (10σ)	(14.1° × 14.1° <i>FWHM</i>)
Balloon gondola and flight	
Gondola total mass: ~600 kg	Gondola dimensions: 1.4 m × 1.4 m × 1.8 m (height)
Flight altitude: 42 km (2.7 g cm ⁻²) at –23° latitude over Brazil	Single flight duration: ≤40 h
Pointing accuracy: ~10 arcmin	Star tracker precision: 10 arcsec

were designed in our lab and the first ten were built in house. A contractor will replicate them for the whole detector plane. Figure 1 shows a photo of one detector and its associated board, as well as an exploded view of the detector system. The detectors are mounted at 45° with respect to the boards to minimize the spacing between adjacent detectors.

The readout circuit of each detector has an applied bias voltage of ~–220 V, a 100 MΩ bias resistor and a 150 nF coupling capacitor. The charge released by an X-ray interaction in each detector will feed an AC-coupled charge-sensitive preamplifier that creates an output pulse of typically ≤1 mV. The pulses are then amplified by ~65 dB by the LNA and formatted by a shaper. A Wilkinson-type eight-bit analog-to-digital converter (ADC) converts the pulse amplitudes to time and then measures this time. The digitized times are proportional to the energy deposited on the detector. This conversion technique is highly linear and precise; we find it is very suitable for CZT detectors with not very high count rates.

Figure 2 shows an energy spectrum of a radioactive ²⁴¹Am source for one detector in the lab. The energy resolution at the 59.5 keV line is 6.6 keV full width at half maximum (FWHM), corresponding to $\Delta E/E = 11\%$. Also shown is a peak from a pulse generator that we used to measure the pulse height spread due to electronic noise. The equivalent electronic noise resolution is 4.5 keV *FWHM*. Since the electronic noise and the Poissonian fluctuations due to the number of charge carriers (electron-hole pairs) within the material must add in quadrature, the intrinsic, purely statistical resolution is 4.8 keV *FWHM* (8%). The red wing on the 60 keV peak is due to incomplete charge collection within the CZT. The spectrum also shows a blend of Cd and Te escape peaks between the radioactive lines.

3.1.2. The scientific data acquisition subsystem

The pulses generated by X-ray interactions in the detectors are processed individually by a data acquisition scheme that includes the front-end analog electronics, as described above, and digital electronics for processing and formatting. The detector pulses are digitized, tagged with position and time, formatted, and then sent to the onboard data-handling computer for storage and transmission to the ground.

The detector signals of each row of 13 detectors in the detector plane array feed into a box with the conversion electronics (CE) with a Complex Programmable Logic Device (CPLD) and microcontrollers. Each one of the 13 CEs acquires data coming from the 13 detector PCBs on that particular row and feeds the pulses into 13 8-bit ADCs (mentioned above), one for each detector, so the energy of each event is determined in 256 channels. The CEs identify the specific detector that is hit on its associated row. Each event will be time-tagged unambiguously with 5 μs precision by an internal clock whose accuracy is checked each second by a GPS receiver. Each CE box receives PPS signals from the GPS.

The signals processed by the CEs will be read by a multiplexing electronics (MUX) box at a rate of 1 Hz. The MUX is thus responsible for identifying the detector in which the event occurred (the event position), the energy and the relative time of the event. For each acquisition cycle (1 s), the MUX will attach the absolute time information coming from the GPS to the data package, so each event will have its instant of occurrence completely determined within 5 μs.

The MUX will send complete datasets containing all data originating in the 13 CEs to the on-board data handling computer

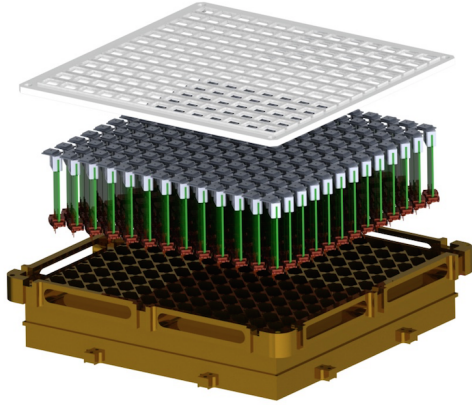
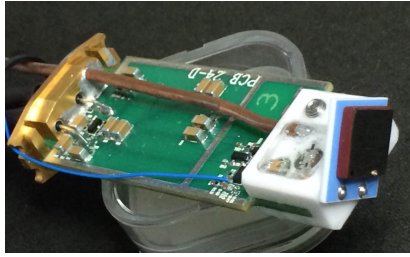


Fig. 1. *Top:* one CZT detector (10 mm × 10 mm × 2 mm) and its associated electronics board with preamp, LNA and shaper. The actual components of the LNA are on the opposite side of the board to avoid electrical interference. The thick wire is the high-voltage supply to the detector (the blue wire is a test lead). *Bottom:* a computer rendering of an exploded view of the detector system. The upper plate is a structural Al frame in which a 0.016 mm-thick aluminum foil will be stretched to provide light and electrical shielding to the detectors. The bottom brass piece provides structure and casing for the detectors and PCBs.

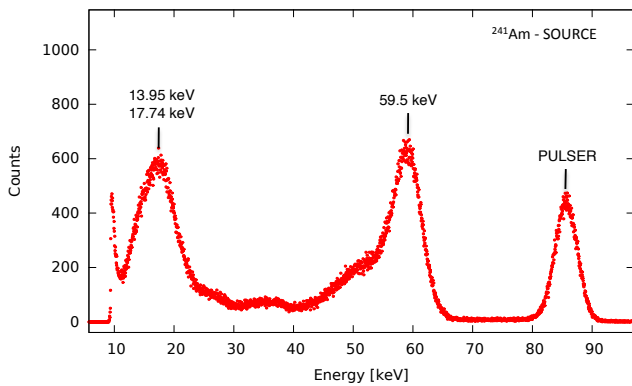


Fig. 2. Energy spectrum of a radioactive ^{241}Am source for one of the CZT detectors. The peak on the right (~ 85 keV) is produced by a pulser and has a FWHM of 4.5 keV. The 59.5 keV peak has a resolution of 6.6 keV FWHM ($\Delta E/E = 11\%$).

(described in Sect. 3.2.1), at a maximum rate of 115 200 bps. In this way, the time, position and energy of each event will be stored individually so that the position and energy distribution of events for any desired integration time can be determined. With an estimated count rate of ~ 55 counts/s for the entire detector plane (see Sect. 4), the dead time will be negligible even for very strong sources at levels of several Crabs.

Figure 3 shows a simplified block diagram of the detector data acquisition subsystem.

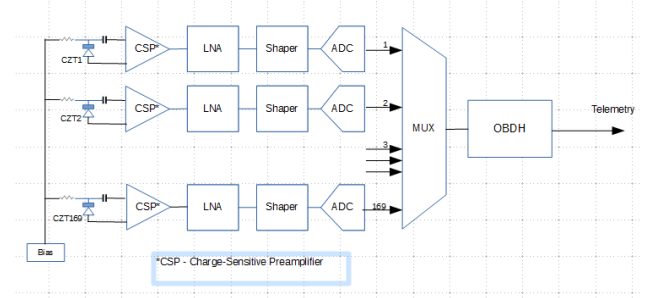


Fig. 3. Simplified block diagram of the detector data acquisition subsystem. The bias voltage is ~ 200 V, the bias resistance is 100 M Ω and the coupling capacitance is 150 nF. LNA: low-noise amplifier; ADC: analog-to-digital converter; MUX: multiplexing electronics; OBDH: onboard data-handling computer.

3.1.3. The collimator

A collimator will be mounted in front of the detector plane in order to define the FOV, minimize background, and provide a uniform illumination fraction of the detectors at any incidence angle. In this way, the entire FOV, all the way to zero intensity, will be fully coded by the mask, ensuring that the experiment does not have any partially coded field of view (PCFOV). Other coded-mask systems do not use collimators, but only shield materials on the sides of the cameras. In these systems, sources in the PCFOV may create severe difficulties in the reconstruction process by casting incomplete shadowgrams of the mask pattern onto the detector plane. In addition, ambiguities in source positions are introduced. We have decided to use a collimator to avoid these problems and reduce background. The price to be paid is the reduction of the sensitivity with increasing off-axis incidence angle, according to the collimator angular response.

The collimator cell centers will be separated by 20 mm in such a way that the individual CZT detectors will each be in the bottom of a collimator cell. The collimator blades are 81-mm high and have lead cores (0.5 mm) and copper plates (0.5 mm) on each side to absorb the radiation impinging at high angles and also provide a graded shield for lead X-ray fluorescence.

The collimator is surrounded by a graded shield made of lead (1.5 mm) in the outside and copper (0.5 mm) in the inside to suppress radiation from outside the FOV. The shielding walls have the same height as the collimator blades (81 mm) and are separated from the last blades by 20 mm, so that the environment that the last detectors (edges and corners) are subjected to is very similar to the more central ones. This is important for minimizing inhomogeneities in the count distribution over the detector plane.

3.1.4. The coded mask

A coded mask, shown in Fig. 4, will be mounted at a distance of 650 mm from the detector plane. The mask has the function of providing a spatial encoding of the X-ray incoming fluxes (see Dicke 1968, for an introduction of the concept). With the knowledge of the mask pattern and the number of X-rays detected by each CZT detector for a given integration time, one can reconstruct an image of the observed FOV by suitable deconvolution or cross-correlation algorithms (Fenimore & Cannon 1978). The mask is made out of 1 mm-thick lead sheets and the basic cells are blue 20 mm × 20 mm squares. The pattern of closed and open elements are a cyclic extension (2×2) of a 13×13 Modified Uniformly Redundant Array (MURA) pattern (Gottesman & Fenimore 1989) with 20 mm-side square

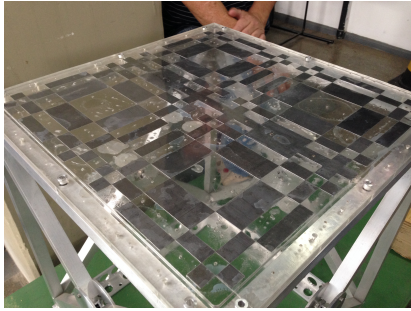


Fig. 4. ProtoMIRAX coded mask. The basic elements are 1mm-thick $20\text{ mm} \times 20\text{ mm}$ lead squares. The basic pattern is a 13×13 MURA repeated four times (2×2) minus 1 row and 1 column to provide unique shadowgrams for any incident direction (skybin). The total size is $500\text{ mm} \times 500\text{ mm}$. The lead pieces are glued to an X-ray transparent, 1 mm-thick acrylic substrate both above and below the mask.

basic cells. Of the 169 elements of the pattern, 84 are open and 85 closed, giving an open fraction of 0.497. In order not to have complete repetitions of the pattern, which would introduce ambiguities in source positions in the sky, we remove one row and one column from the total 2×2 array of basic patterns, so that the final dimensions of the mask are 25×25 elements or $500\text{ mm} \times 500\text{ mm}$.

The MURA patterns belong to a class of aperture patterns that allow images to be produced with no intrinsic noise, which means that the autocorrelation function of the mask pattern is a delta function. (Actually, to be precise, the delta function is the result of the cross-correlation between the mask pattern and the decoding function, which is almost exactly equal to the mask pattern with the exception of one single element.) For a point source, the reconstructed image is “perfect” in the sense that it produces a peak in an otherwise completely flat image (see [Gottesman & Fenimore 1989](#) and [Braga et al. 2002](#) for details about imaging with MURAs). With this configuration, the protoMIRAX X-ray camera will have a total FOV of $20^\circ 8' \times 20^\circ 8'$ totally coded by the mask and a geometrical angular resolution (one skybin) of $1^\circ 43'$. Because there are 10 mm gaps between adjacent detectors, the fraction of the FOV with maximum sensitivity (total detector area illuminated) will be $7^\circ 03' \times 7^\circ 03'$. In other words, the collimator blades will only start shadowing the detectors for incident directions outside this angular range, centered on the camera axis. The source location accuracy (see [Caroli et al. 1987](#)) will depend on the incident angle and will be limited by the precision of the pointing system. In the best case, it will be around $10'$ for a 10σ source in the center of the FOV.

3.1.5. The passive shield

The detector array and associated electronics, including the detector boards, power supplies and batteries, will be surrounded on the sides and bottom by a gradual passive shield of lead (1.5 mm) and copper (0.5 mm). This shield will be responsible for absorbing most of the radiation coming from directions other than those defined by the collimator. Figure 5 shows computer diagrams with the main parts of the XRC, including the aluminum support structures.

3.2. The balloon gondola

The protoMIRAX balloon gondola will house the X-ray camera and the various subsystems of the space segment,

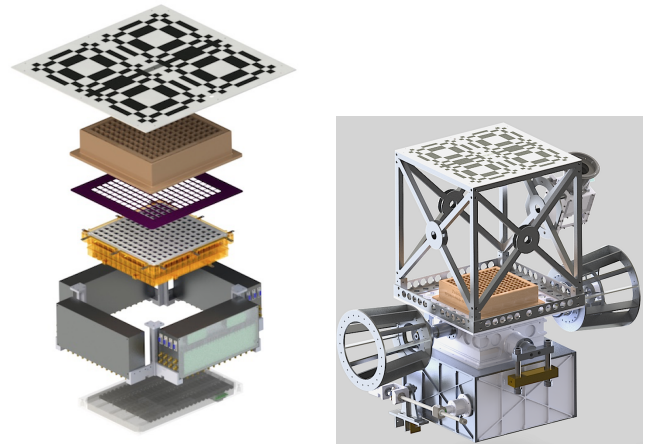


Fig. 5. Computer rendering of the protoMIRAX X-ray Camera. *Left:* exploded diagram of the XRC, showing, from top to bottom, the coded mask, collimator, aluminum foil support plate, detector system, detector electronics and power supply boxes, and battery pack. *Right:* the assembled XRC with passive shielding and structural parts, including the elevation axis support. Also shown are one of protoMIRAX’s two star cameras (top right) and the elevation driving mechanism (bottom left) based on a ball screw.

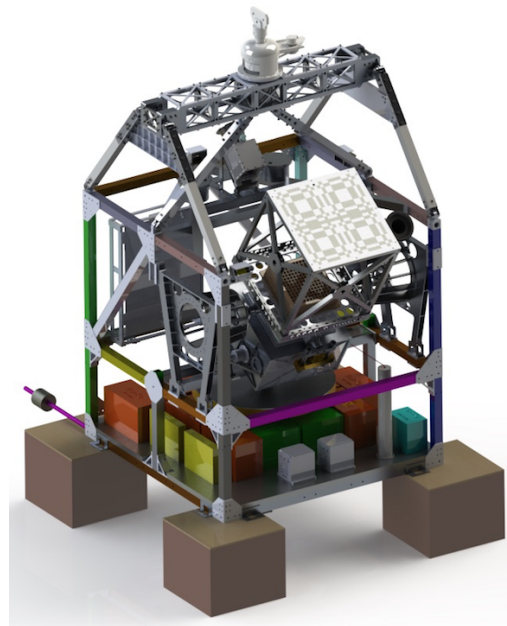


Fig. 6. Computer rendering of the protoMIRAX balloon gondola, showing the X-ray camera on the front side. The colored boxes at the bottom of the frame are battery packs and electronics racks. The flat box in the back is the TM&TC subsystem. The reaction wheel can be seen below the XRC. One can also see the two star cameras: one is fixed at the XRC and the other (behind the coded mask) is fixed in the gondola frame. At the top, the decoupling mechanism that connects to the balloon cables is shown. The four brown boxes in the bottom are crash pads. The gondola frame dimensions are $1.4\text{ m} \times 1.4\text{ m} \times 2\text{ m}$.

including the On-Board Data Handling Subsystem (OBDH), the Attitude Control and Pointing Subsystem (ACS), the Telemetry and Command Subsystem (TM&TC), and the Power Supply Subsystem (PSS). Also, there will be a main GPS receiver that will provide universal time to all subsystems and two star cameras that will be part of the control loop. A computer rendering of the gondola is shown in Fig. 6.

The gondola will use a power supply system based on packages of Li-ion batteries. A telemetry system operating in the *L* band (1.5 GHz) will provide data and housekeeping links to the ground. A command system will provide pointing operations during the balloon flight. The science data will be stored on-board on computer flash memories and will also be entirely transmitted to the ground.

3.2.1. The On-Board Data Handling Subsystem

The On-Board Data Handling Subsystem (OBDH) is responsible for acquiring, formatting and transmitting all data that come from the various subsystems of protoMIRAX's space segment to the ground station (GS). The OBDH is also responsible for receiving and retransmitting the various commands sent by the GS to the gondola, when necessary. For each X-ray photon detected by the XRC, a six-byte packet is created encasing the time stamp, x - y position (detector that was hit) and energy (pulse height) of the event that were formatted and sent by the MUX. These event packets are then sent every one second to the OBDH through a 115.2 kbps RS-422 unidirectional serial communication line. In addition, another 115.2 kbps RS-422 serial interface allows OBDH to send specific commands to the XRC and receive XRC's housekeeping data.

We devised a cost-effective and robust solution for the experiment timing in which a single Global Positioning System (GPSDXA) unit sends PPS (1 pulse per second) and data to the various subsystems of the experiment: OBDH, XRC, ACS, and the Autonomous Star Trackers (AST). The OBDH attaches the UT data from the GPSDXA to the scientific data files at each second, so absolute timing information at the resolution of $5 \mu\text{s}$ can be retrieved for every event.

The OBDH also communicates with the GS and the ACS. A 500 kbps synchronous communication channel connects the OBDH with the Flight Control and Telecommunications Subsystem (FCTS). This channel is exclusively dedicated to transmit scientific data to the GS. The FCTS also communicates with the GS via a double transmitter/receiver system operating in the *L* band. To transmit all housekeeping data generated by the several subsystems of the space segment, the OBDH uses a serial RS-232 channel operating at 115.2 kbps. Ground station commands are received by the OBDH via FCTS by means of a 9.6 kbps RS-232 serial channel. In addition, all ACS data are sent to the OBDH prior to be sent to the GS via another 115.2 kbps RS-422 serial interface standard.

The main hardware unit of OBDH is the Payload Data Handling Computer (PDCpM), which is a PC/104 ultra-low-power AMD Geode LX computer. It operates on 333 MHz, has a 128-MByte SDRAM, and has all the necessary interfaces previously mentioned in addition to analog-digital/digital-analog converters. The PDCpM went through thermal cycling and thermal vacuum testing with temperatures ranging from -40°C to $+85^\circ\text{C}$ and pressure as low as 1.3 mbar.

The software embedded in the computer (SWPDCpM) has been developed in C language over the real-time operating system RTEMS. The architecture of the SWPDCpM is composed of three layers where the bottom layer is the basic software, the intermediate layer is the flight software library in which there are basic services and reusable components, and the top layer is the application software, the main part of SWPDCpM.

Figure 7 shows a simplified physical architecture of the protoMIRAX experiment with its main subsystems.

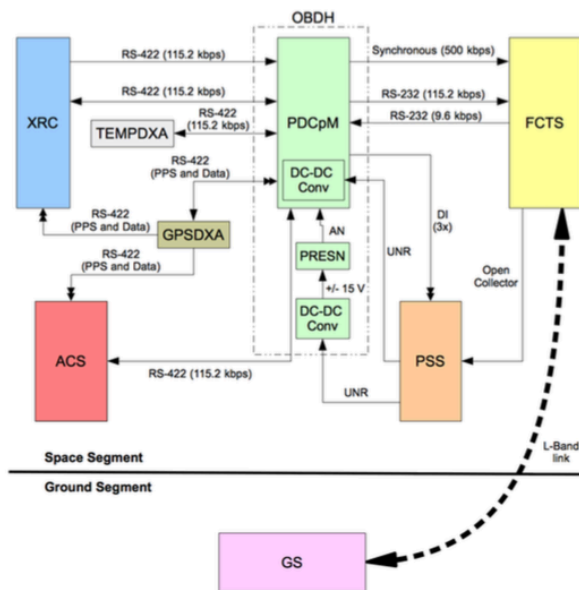


Fig. 7. Simplified physical architecture of the protoMIRAX balloon experiment. XRC: X-ray camera; ACS: Attitude Control System; TEMPDXA: Temperature monitoring equipment; GPSDXA: GPS unit; OBDH: On-Board Data Handling Subsystem; PDCpM: Payload Data Handling Computer; DC-DC Conv: DC-DC Converter; PRESN: Pressure Sensor; PSS: Power Supply Subsystem; FCTS: Flight Control and Telecommunications Subsystem.

3.2.2. The Attitude Control and Pointing Subsystem

The X-ray camera will be placed in an alt-azimuth mount in the balloon gondola, allowing pointing to different targets in the sky and tracking them continuously down to elevation angles of 30° . A ball screw mechanism, with a step motor, will allow smooth and secure motion in elevation, and the azimuth motion will be provided by a system that rotates the entire gondola with respect to the geomagnetic field and the positions of the sun and the stars in the sky. The attitude control system will employ several sensors and actuators. The sensors include an electronic compass, an accelerometer, two star sensors, a sun tracker and both azimuth and elevation angular encoders. The actuators include a reaction wheel for angular momentum exchange and dump, and motors that will drive the motions in both elevation and azimuth. The gondola also has a mechanism at its top for decoupling its rotation with respect to the balloon itself and a motor for desaturating the reaction wheel. The overall pointing accuracy of the control system is $\lesssim 0.5^\circ$, depending on the elevation angle. High elevations are in general more difficult to control since small changes in the pointing direction near the zenith leads to large azimuthal and roll angle displacements. Also, the accuracy will depend on whether the flight is at daytime or nighttime. At night, the star cameras will provide more accurate control.

The two autonomous star sensors of protoMIRAX are being developed at INPE. They are wide-field ($25^\circ \times 25^\circ$) optical (400–800 nm) cameras with a 35 mm focal length. The imaging sensor is a CMOS APS (active pixel sensor) with 1024×1024 pixels and quantum efficiency up to 25%. An especially designed algorithm for star pattern recognition provides attitude knowledge precision better than ten arcseconds (1σ) around the cross-foresight axes (yaw and pitch) and better than 60 arcsec (1σ) around the foresight axis (roll angle). One of the star sensors is fixed in the XRC mechanical frame so that it aids in the precise pointing of the XRC telescope. Its optical axis is

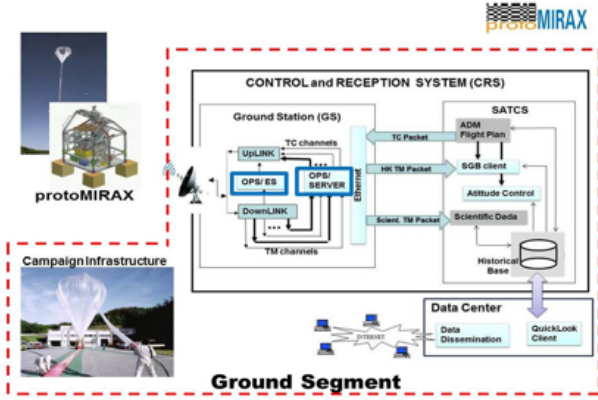


Fig. 8. Physical architecture of the protoMIRAX ground subsystem.

tilted 24° with respect to the X-ray axis towards lower elevations, so as to avoid having the balloon in the FOV for high-elevation observations. Even with this misalignment, there will be occasions when the primary star tracker will be obstructed by the balloon. In these cases the XRC attitude will be determined by the secondary star tracker mounted in the gondola, albeit with a somewhat reduced accuracy due to uncertainties from the angular encoders used in the motors that control the XRC mechanical frame elevation. The star trackers are also capable of acquiring images, which will be used for evaluation of the star tracker performance during the flight.

3.3. The ground subsystem

The operations of the protoMIRAX telescope during the balloon flights will make use of the ground facilities already available at INPE. The reuse strategy focused on two subsystems: (i) the balloon flight control (OPS) and (ii) the experiment operation itself, which will be supported by the SATellite Control System (SATCS). SATCS is a software-based architecture developed at INPE for satellite commanding and monitoring. Considering that protoMIRAX is a pathfinder for the MIRAX satellite mission, a ground infrastructure compatible with INPE's satellite operation approach would be useful and is highly recommended for controlling and monitoring the experiment during the balloon campaigns.

The OPS required investments on information technology. The available balloon GS needed little hardware maintenance, but significant efforts on software updating were necessary. The original stand-alone computer system dedicated to run the flight control software was modernized both in hardware and software by the new system named OPS/ES. In addition, a new server computer, properly configured for Ethernet connections, has extended the existing GS facilities with a network switch, serial converters and a new piece of software named OPS/Server in order to support the available uplink and downlink channels being mapped to TCP/IP gateways. Those communication improvements were necessary to support the interoperability between the balloon GS, SATCS, and protoMIRAX data center.

Some effort in software customization was necessary because SATCS architecture complies with particular operational requirements on different missions by using several customized object-oriented software elements and frameworks. The diagram in Fig. 8 shows the ground solution designed for the ground segment of the protoMIRAX experiment.

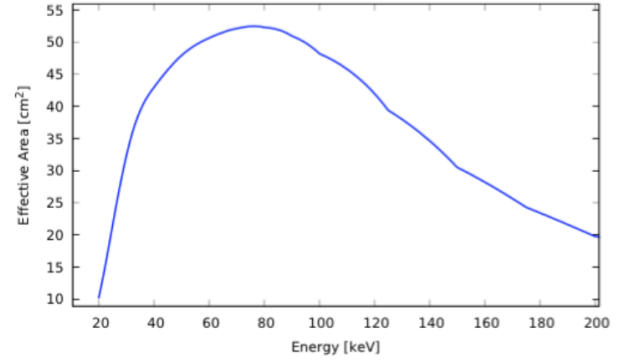


Fig. 9. Effective area of protoMIRAX.

4. Effective area and sensitivity

The effective area of a balloon experiment for the observation of cosmic sources is a function of energy (E), atmospheric depth and zenith angle:

$$A_{\text{eff}}(E) = A_{\text{geo}} \epsilon e^{-(\mu/\rho)_A x \sec z} \quad (1)$$

where A_{geo} is the geometrical detection area, $\epsilon \equiv 1 - \exp(-\mu_D l)$ is the detector efficiency, $\mu_D(E)$ is the detector's attenuation coefficient in cm^{-1} , l is the detector thickness in cm, $(\mu/\rho)_A(E)$ is the attenuation coefficient of the atmosphere in cm^2/g , x is the atmospheric depth in g cm^{-2} and z is the zenith angle.

For the expected observations of protoMIRAX at 2.7 g cm^{-2} , considering a point source at the zenith, the effective area is shown in Fig. 9, with a maximum value of 52 cm^2 at $\sim 80 \text{ keV}$. It is important to note that the geometrical area for a point source at infinity is the total detector area of 169 cm^2 multiplied by the open fraction of the mask, which is 0.497 (see Sect. 3.1.4).

The sensitivity of the experiment can be calculated by estimating the background at the altitudes expected for the balloon flight. This was produced by performing Monte Carlo simulations using the software package GEANT4 (Agostinelli et al. 2003), a well-known suite of routines that performs detailed calculations of gamma-ray and particle interactions on all materials. Given the experiment mass model and the environmental particle and photon fields, the code provides the detector spectral response, both prompt and delayed.

Based on detailed GEANT4 calculations we carried out (Penacchioni et al. 2015; Castro et al., in prep.), the estimated background count rate for the entire detector plane, in the 30 to 200 keV energy range, is of $\sim 55 \text{ counts/s}$. In these simulations, we considered both the anisotropic atmospheric X and γ -ray spectra and the cosmic diffuse contribution coming from the telescope aperture. We also considered primary and secondary protons, electrons and neutrons. As shown by Penacchioni et al. (2015), the photon contribution is dominant up to 90 keV, where the contribution due to protons becomes almost equally important. Neutrons are important below 35 keV and the electron contribution is negligible.

In Fig. 10 we show a map of the simulated background counts over the detector plane for an integration of four hours at 2.7 g cm^{-2} for the entire energy range 30–200 keV. The increased count rates at the edges and corners of the detector plane are most likely due to the closeness of these detectors with the shielding materials and support structures, which produce secondary radiation by scattering. Another factor could be due to the extra shielding produced by the collimator blades to the detector in the central areas of the detector plane.

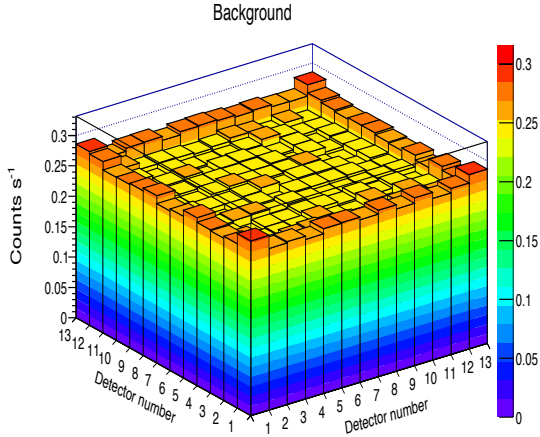


Fig. 10. Background count distribution over the detection plane in the detector energy range 30–200 keV, for an observation time of 4 h at balloon altitudes.

Taking the expected background levels at balloon altitudes as a function of energy, one can calculate the sensitivity of the experiment in terms of the minimum detectable flux at a particular statistical significance. As shown by [Gottesman & Fenimore \(1989\)](#), the signal-to-noise ratio ($S/N \equiv N_\sigma$) of a coded mask instrument that uses URAs or MURAs, for a single point source, is given by

$$N_\sigma = \frac{N_S}{\sqrt{2N_S + N_B}}, \quad (2)$$

where N_S is the net source counts and N_B is the background number of counts for a given integration time in a particular energy range. Solving for N_S , one gets

$$N_S = N_\sigma \left(N_\sigma + \sqrt{N_\sigma^2 + N_B} \right). \quad (3)$$

If we are interested in a minimum detectable flux, the signal-to-noise ratio will be a small number ($\lesssim 10$), and it is reasonable to assume that $N_\sigma^2 \ll N_B$ for sufficiently long integration times. Therefore, $N_S \approx N_\sigma \sqrt{N_B}$.

Now, if S is the source flux in photons $\text{cm}^{-2} \text{s}^{-1} \text{keV}^{-1}$, then $N_S = S A_{\text{eff}} T \Delta E$, where A_{eff} is the effective area in cm^2 , T is the integration time in seconds and ΔE is the energy interval under consideration (in keV). Similarly, $N_B = B A_{\text{geo}} T \Delta E$, where B is the background level in the more suitable units of counts $\text{cm}^{-2} \text{s}^{-1}$ and A_{geo} is the geometrical area of the whole detector plane.

The minimum source flux that will be detectable at a level of N_σ will then be

$$F_{\text{min}} = \frac{N_\sigma}{A_{\text{eff}} \Delta E} \sqrt{\frac{B A_{\text{geo}}}{T}} \text{ photons cm}^{-2} \text{s}^{-1} \text{keV}^{-1}. \quad (4)$$

According to this expression, the 3σ sensitivity (minimum detectable flux) for the whole energy band is found to be approximately 1.9×10^{-5} counts $\text{cm}^{-2} \text{s}^{-1}$ from 30 to 200 keV, considering 8 h of integration at 2.7 g cm^{-2} and a zenith angle of 30° . This allows protoMIRAX to make detailed observations of the Crab (even at low elevation angles) and also detect a few X-ray binaries in states of high hard X-ray emission. In [Fig. 11](#) we show a 3σ sensitivity curve for protoMIRAX for an integration time of eight hours at 2.7 g cm^{-2} , considering a point source at

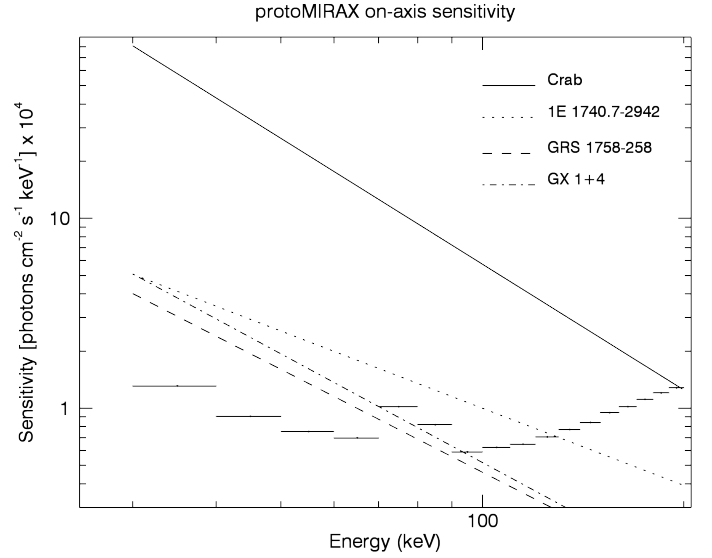


Fig. 11. On-axis sensitivity curve for protoMIRAX. The horizontal bars are the minimum detectable fluxes at a level of 3σ at an atmospheric depth of 2.7 g cm^{-2} and a zenith angle of 30° . The integration time is 8 hours. Also shown are the spectra of 4 X-ray sources that will be observed in the first balloon flight. The source spectra were taken from [Sizun et al. \(2004; Crab\)](#), [Grebenev et al. \(1995; 1E 1740.7–2942\)](#), [Sunyaev et al. \(1991b; GRS 1758–258\)](#) and [Dieters et al. \(1991; GX 1 + 4\)](#).

a zenith angle of 30° . The increased minimum flux values between 70 and 90 keV are due to somewhat strong lead fluorescent lines (reported by [Penacchioni et al. 2015](#)) in the estimated background spectrum. We are in the process of studying different shielding configurations that will very likely minimize this problem.

5. Image simulation

To predict the performance of the protoMIRAX imaging system, we have simulated an observation of the Crab nebula during a meridian transit at our flight latitudes (23° S). To calculate the number of counts from the source, we have considered the zenith angle variation with time before and after the transit, which occurs at an elevation of 45° . Based on the Crab hard X-ray spectrum taken from [Sizun et al. \(2004\)](#), we used GEANT4 to build a simulated shadowgram of a Crab observation in the center of the FOV, which is shown in [Fig. 12](#).

The image covers the entire FOV of $21^\circ \times 21^\circ$, and each sky bin corresponds to $1^\circ 43'$ of the sky. The overall S/N of the image is 109σ (see [Penacchioni et al. 2015](#), for details). This value corresponds to 91% of the theoretical value given by expression (2) above. The loss in detection significance is mainly due to the non-uniformity of the background across the detector plane. In [Fig. 13](#) we show the reconstructed Crab image. It is interesting to note that the Crab will in principle be observable by protoMIRAX at a 5σ level for an integration as short as 63 s, which makes it a very good calibration source for the experiment.

6. Conclusion

The protoMIRAX experiment is a balloon-borne hard X-ray telescope being developed as a scientific and technical pathfinder for the MIRAX satellite mission. In the current configuration, which is under revision owing to restrictions imposed by

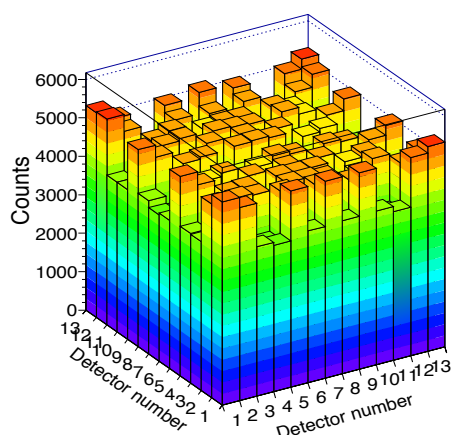


Fig. 12. Count distribution (shadowgram) on the detector plane of a simulated observation of the Crab, including the expected background, for an integration time of 4 h around the meridian passage at a latitude of 23° S. The energy range is 30 to 200 keV.

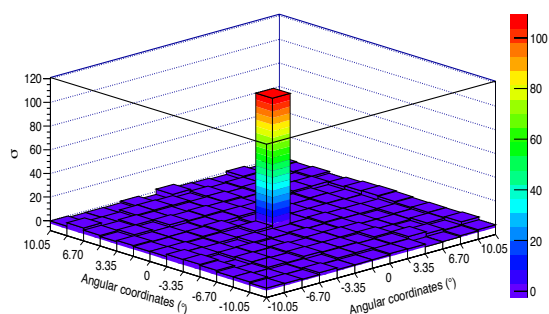


Fig. 13. Simulated image of the Crab nebula region for an integration time of 4 h around the meridian transit at balloon altitudes (2.7 g cm^{-2}). The energy range is 30–200 keV. The S/N of the detection is 109.

the Brazilian space program, MIRAX will consist in a set of wide-field coded-mask hard X-ray cameras (5–200 keV) with an angular resolution of $\sim 5\text{--}6$ arcmin that will operate in scanning mode in a near-equatorial circular low-Earth orbit. MIRAX main goals include the characterization, with unprecedented depth and time coverage, of a large sample of variable and transient phenomena on accreting neutron stars and black holes, as well as active galactic nuclei and GRBs.

Apart from serving as a testbed for several MIRAX subsystems, protoMIRAX will be capable of doing interesting science of its own. The hard X-ray camera, similar to the hard X-ray imager being developed for MIRAX, albeit with a much lower angular resolution and smaller detector area, has a resolution of $1^\circ 43'$ with a fully coded FOV of $21^\circ \times 21^\circ$. Detailed background calculations were performed with the GEANT4 package, and the expected background at balloon altitudes at a latitude of -23° over the SAA region in Brazil provides a 3σ sensitivity for the 30–200 keV range of $\sim 1.9 \times 10^{-5}$ photons $\text{cm}^{-2} \text{s}^{-1}$ for an integration of eight hours. In its first balloon flight, protoMIRAX

will observe the Crab nebula for calibration and imaging demonstration and also the GC region for scientific purposes. The experiment is in a very advanced state of development and we hope to carry out the first balloon flight in late 2015.

Acknowledgements. We thank FINEP, CNPq and FAPESP, Brazil, for financial support. We also thank Fernando G. Blanco, Sérgio Admirabile, Luiz A. Reitano, Wendell P. da Silva, Leonardo Pinheiro, Fernando Orsatti, Paulino Scherer and the engineers from the company COMPSIS in São José dos Campos for invaluable technical support. A.V.P. acknowledges the support by the international Cooperation Program CAPES-ICRANET financed by CAPES – Brazilian Federal Agency for Support and Evaluation of Graduate Education within the Ministry of Education of Brazil. M.C.A. and J.R.S. also acknowledge CAPES for Ph.D. and post-doctoral fellowships, respectively.

References

- Agostinelli, S., Allison, J., Amako, K., et al. 2003, *Nucl. Instrum. Methods Phys. Res. A*, **506**, 250
- Braga, J., D'Amico, F., Villela, T., et al. 2002, *Rev. Sci. Instrum.*, **73**, 3619
- Braga, J., Rothschild, R., Heise, J., et al. 2004, *Adv. Space Res.*, **34**, 2657
- Bühler, R., & Blandford, R. 2014, *Rep. Prog. Phys.*, **77**, 066901
- Caroli, E., Stephen, J. B., Di Cocco, G., Natalucci, L., & Spizzichino, A. 1987, *Space Sci. Rev.*, **45**, 349
- Castro, M., D'Amico, F., Braga, J., et al. 2014, *A&A*, **569**, A82
- Dicke, R. H. 1968, *ApJ*, **153**, L101
- Dieters, S. W. B., Greenhill, J. G., Sharma, D. P., et al. 1991, *Adv. Space Res.*, **11**, 35
- Fenimore, E. E., & Cannon, T. M. 1978, *Appl. Opt.*, **17**, 337
- Gehrels, N., & Swift Team. 2004, *New Astron. Rev.*, **48**, 431
- González-Galán, A., Kuulkers, E., Kretschmar, P., et al. 2012, *A&A*, **537**, A66
- Gottesman, S. R., & Fenimore, E. E. 1989, *Appl. Opt.*, **28**, 4344
- Grebenev, S. A., Pavlinsky, M. N., & Sunyaev, R. A. 1995, *Adv. Space Res.*, **15**, 115
- Harrison, F. A., Craig, W. W., Christensen, F. E., et al. 2013, *ApJ*, **770**, 103
- Jager, R., Mels, W. A., Brinkman, A. C., et al. 1997, *A&AS*, **125**, 557
- Kuznetsov, S., Gilfanov, M., Churazov, E., et al. 1996, in *Roentgenstrahlung from the Universe*, eds. H. U. Zimmermann, J. Trümper, & H. Yorke, 157
- Levine, A. M., Bradt, H., Cui, W., et al. 1996, *ApJ*, **469**, L33
- Liang, E. P., & Nolan, P. L. 1984, *Space Sci. Rev.*, **38**, 353
- Madsen, K. K., Reynolds, S., Harrison, F., et al. 2015, *ApJ*, **801**, 66
- Makishima, K., Ohashi, T., Sakao, T., et al. 1988, *Nature*, **333**, 746
- Masetti, N., Orlandini, M., Palazzi, E., Amati, L., & Frontera, F. 2006, *A&A*, **453**, 295
- Mirabel, I. F., Rodriguez, L. F., Cordier, B., Paul, J., & Lebrun, F. 1992, *Nature*, **358**, 215
- Nagase, F. 1989, *PASJ*, **41**, 1
- Paul, J., Ballet, J., Cantin, M., et al. 1991, *Adv. Space Res.*, **11**, 289
- Penacchioni, A. V., Braga, J., Castro, M. A., & D'Amico, F. 2015, *J. High Energy Astrophysics*, in press
- Ricker, G. R., Atteia, J.-L., Crew, G. B., et al. 2003, in *Gamma-Ray Burst and Afterglow Astronomy 2001: A Workshop Celebrating the First Year of the HETE Mission*, eds. G. R. Ricker, & R. K. Vanderspek, *AIP Conf. Ser.*, **662**, 3
- Sizun, P., Shrader, C. R., Attié, D., et al. 2004, in *5th INTEGRAL Workshop on the INTEGRAL Universe*, eds. V. Schoenfelder, G. Lichti, & C. Winkler, *ESA SP*, **552**, 815
- Sunyaev, R. A., Babichenko, S. I., Goganov, D. A., Tabaldyev, S. R., & Iamburenko, N. S. 1990, *Adv. Space Res.*, **10**, 233
- Sunyaev, R., Churazov, E., Gilfanov, M., et al. 1991a, *ApJ*, **383**, L49
- Sunyaev, R., Gilfanov, M., Churazov, E., et al. 1991b, *Sov. Astron. Lett.*, **17**, 50
- Takahashi, T., Mitsuda, K., Kelley, R., et al. 2014, in *SPIE Conf. Ser.*, **9144**, 25
- Tavani, M., Bulgarelli, A., Vittorini, V., et al. 2011, *Science*, **331**, 736
- Virgili, E., Frontera, F., Valsan, V., et al. 2013, in *SPIE Conf. Ser.*, **8861**, 7
- Wilson-Hodge, C. A., Cherry, M. L., Case, G. L., et al. 2011, *ApJ*, **727**, L40
- Winkler, C. 1995, *Exp. Astron.*, **6**, 71